Radboud Repository

Radboud University Nijmegen

PDF hosted at the Radboud Repository of the Radboud University Nijmegen

The following full text is a publisher's version.

For additional information about this publication click this link.
http://hdl.handle.net/2066/132496

Method for high precision reconstruction of air shower X_{max} using two-dimensional radio intensity profiles

S. Buitink,[1] A. Corstanje,[1] J. E. Enriquez,[1] H. Falcke,[1,2,3,4] J. R. Hörandel,[1,3] T. Huege,[5] A. Nelles,[1] J. P. Rachen,[1] P. Schellart,[1] O. Scholten,[6] S. ter Veen,[1] S. Thoudam,[1] and T. N. G. Trinh[6]

[1]*Department of Astrophysics/IMAPP, Radboud University Nijmegen, 6500 GL Nijmegen, Netherlands*
[2]*Netherlands Institute for Radio Astronomy (ASTRON), Postbus 2, 7990 AA Dwingeloo, Netherlands*
[3]*Nikhef, Science Park Amsterdam, 1098 XG Amsterdam, Netherlands*
[4]*Max-Planck-Institut für Radioastronomie, Auf dem Hügel 69, 53121 Bonn, Germany*
[5]*IKP, Karlsruhe Institute of Technology (KIT), Postfach 3640, 76021 Karlsruhe, Germany*
[6]*KVI CART, University of Groningen, 9747 AA Groningen, Netherlands*
(Received 28 August 2014; published 17 October 2014)

The mass composition of cosmic rays contains important clues about their origin. Accurate measurements are needed to resolve longstanding issues such as the transition from Galactic to extra-Galactic origin and the nature of the cutoff observed at the highest energies. Composition can be studied by measuring the atmospheric depth of the shower maximum X_{max} of air showers generated by high-energy cosmic rays hitting the Earth's atmosphere. We present a new method to reconstruct X_{max} based on radio measurements. The radio emission mechanism of air showers is a complex process that creates an asymmetric intensity pattern on the ground. The shape of this pattern strongly depends on the longitudinal development of the shower. We reconstruct X_{max} by fitting two-dimensional intensity profiles, simulated with CoREAS, to data from the Low Frequency Array (LOFAR) radio telescope. In the dense LOFAR core, air showers are detected by hundreds of antennas simultaneously. The simulations fit the data very well, indicating that the radiation mechanism is now well understood. The typical uncertainty on the reconstruction of X_{max} for LOFAR showers is 17 g/cm^2.

I. INTRODUCTION

High-energy cosmic rays are routinely measured by experiments around the world, yet there are still many urgent questions about their origin. Cosmic rays below 10^{16} eV are expected to be of Galactic origin, while the highest-energy cosmic rays are likely to come from extra-Galactic sources. However, it is not known how and at what energy this transition takes place. Another important question is whether the cutoff at the end of the spectrum [1,2] is due to interactions of cosmic-ray protons with the cosmic microwave background [3,4] or marks the highest energy that cosmic accelerators can reach. Accurate measurements of the cosmic-ray mass composition can resolve these questions [5]. In addition, a clean separation between protons and heavy nuclei above 6×10^{19} eV will greatly improve the search for a correlation between cosmic-ray arrival directions and their sources [6]. The fluorescence detection technique yields an excellent precision of ~ 20 g/cm^2 [7,8], but its low duty cycle limits the detection rate at the highest energies.

Several techniques exist to measure mass-sensitive shower parameters. Particle detector arrays like KASCADE-Grande [9] and IceTop [10] measure the electron-to-muon ratio of the secondary shower particles at ground level. This ratio depends on the mass of the primary particle but also on the age of the shower, which makes the technique susceptible to shower-to-shower fluctuations.

The mass composition can also be inferred from the distribution of X_{max}, the atmospheric depth of the shower maximum. At the Pierre Auger observatory, the longitudinal shower profile is measured by observing the fluorescence light that is emitted by air molecules that were excited by shower particles [7]. Alternatively, X_{max} can be inferred by measuring the optical Cherenkov light emitted by the shower particles with arrays like Tunka [11]. Both techniques require dark nights and are therefore severely limited in duty cycle (below 15%). The fluorescence technique yields the best precision on X_{max} of ~ 20 g/cm^2.

Here, we propose a new technique that has the same precision but has a duty cycle of almost 100%, based on the radio emission produced by air showers. Like fluorescence light, the radio signal carries information of the complete longitudinal development of the shower [12]. It is therefore possible to reconstruct X_{max} from the radio signal [13]. The method presented here requires measurements with many radio antennas simultaneously, in order to adequately sample the radiation profile. We apply this technique to data from the Low Frequency Array (LOFAR) radio telescope [14–16].

Our reconstruction technique requires precise simulations of the radio emission. The theory of air-shower radio emission has developed rapidly in the last decade, and simulation codes based on different approaches are now converging toward similar results [17]. In this work, we use

the CoREAS simulation package [18], which is a plugin for CORSIKA [19] that computes the radio pulse by adding the contribution of all individual electrons and positrons in the shower. We demonstrate that simulations are in excellent agreement with the LOFAR measurements, which sample the radio emission with hundreds of antennas per individual shower.

Section II gives a brief introduction to the LOFAR radio telescope array. In Sec. III, we describe the simulation tools and settings. The new reconstruction technique is explained in Secs. IV and V contains a review of systematic effects in the reconstruction. Conclusions are given in the final section.

II. LOFAR

LOFAR is a new-generation radio telescope constructed in the north of the Netherlands with satellite stations across Europe. It consists of thousands of dipole antennas, sensitive in the frequency range of 10–240 MHz. LOFAR has a flexible design that allows many different observation modes, some of which can run simultaneously. The raw electromagnetic waveform as it is measured by the dipoles is stored for 5 sec on ring buffers for each active antenna.

LOFAR is organized in stations, each containing 96 low-band antennas (LBAs; 10–90 MHz) and 48 high-band antennas (HBAs; 110–240 MHz). In the center of LOFAR, six of these stations are placed close together on a small artificial island, called the *superterp* (see Fig. 1). Other stations are placed around this island at increasing distances. A total of 24 stations form the LOFAR core, which has a diameter of ~2 km. For cosmic-ray detection, we focus on this dense core region.

The core is augmented with the LOFAR Radboud Air Shower Array (LORA) [20], which comprises 20 particle detectors. They cover the superterp area and are an essential part of the cosmic-ray measurement capability. LORA detects air showers above 10^{16} eV and provides a trigger for the radio antennas. It reconstructs the arrival direction, core position and gives a first energy estimate of the shower. Radio pulses can unambiguously be associated to air showers when their arrival time and direction coincides with the LORA reconstruction. Triggering on the radio pulse itself is technically possible, but an online filter is needed to distinguish cosmic-ray pulses from anthropogenic background noise. This is a subject of future study.

When a LORA trigger is received, a 2 ms trace is read out from the ring buffers of all active antennas and stored for offline processing [15]. A radio signal is typically found in hundreds of antennas. Depending on the mode of the current astronomical observations, either LBA or HBA data are available. Since HBA data are more challenging to analyze [21], we only consider LBA data in this study.
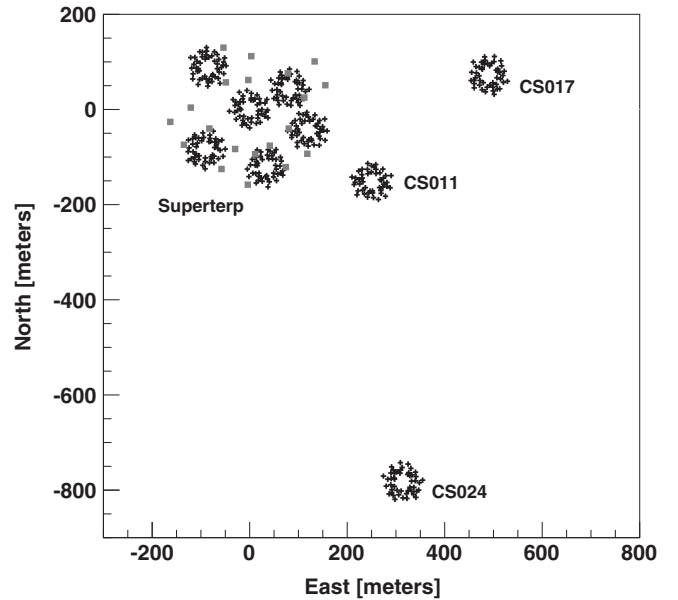

FIG. 1. Part of the LOFAR core. The "+" signs indicate the positions of antennas that are arranged in stations. Only the LBA antennas in the outer rings of each station are plotted. The inner parts of the LBA stations and the HBA stations, which are not used in this study, are not included in the plot. The central six stations form the superterp. Other core stations lie at increasingly larger distances from this cluster, three of which are visible in the map. The grey squares indicate the positions of LORA detectors.

III. RADIO EMISSION SIMULATIONS

A. Emission mechanism

The dominant component of the radio emission of air showers is driven by the geomagnetic field [16,22]. The electrons and positrons are deflected in opposite directions by the Lorenz force, and their drift creates a current perpendicular to the shower axis. As the shower develops, this current first grows and then decays, producing radio emission. The radiation is linearly polarized in the $\mathbf{v} \times \mathbf{B}$ direction, where $\mathbf{v}$ is the velocity of the shower front and $\mathbf{B}$ is the Earth's magnetic field.

As the shower propagates through the atmosphere, it also develops an excess of negative charge, due to knockout electrons from atmospheric molecules joining the shower and the annihilation of positrons. The growth and subsequent decay of the charge excess give rise to a secondary emission component [23]. Charge excess radiation is also linearly polarized, but in a different direction, pointing radially outward from the shower axis. The relative contribution of charge excess to the total emission depends on the geometry (angle to the geomagnetic field, zenith angle, observer position, etc.) and has typical values of 5%–20% of the total pulse amplitude [24–26].

Because geomagnetic and charge excess radiation are polarized in different directions, the total emission is found by adding these contributions vectorially. The radiation

profile can be easiest understood when it is plotted in the shower plane, with axes in the direction of $\mathbf{v} \times \mathbf{B}$ and $\mathbf{v} \times (\mathbf{v} \times \mathbf{B})$ (see Fig. 3). In this frame, there is total constructive interference between the two components along the $\mathbf{v} \times \mathbf{B}$ axis in the positive direction, while the interference is most destructive in the negative direction along the same axis. Along the $\mathbf{v} \times (\mathbf{v} \times \mathbf{B})$ axis, the two components are polarized orthogonally and add in quadrature.

The resulting interference pattern is not rotationally symmetric and is typically bean shaped. Evidently, the lateral distribution of the radio pulse power is not a one-dimensional function of the distance to the shower axis. The radio profile can only be accurately described in two dimensions.

The bulk of the shower particles is confined to the shower front, a thin disk that travels toward the Earth at relativistic speed. For wavelengths exceeding the disk thickness (several meters), the radiation will be coherent (up to ~100 MHz). However, the propagation of the radio emission in a dielectric medium (air has an index of refraction of $n \approx 1.0003$ at sea level) produces Cherenkov-like effects, which must be included to properly describe the radiation [27]. At the Cherenkov angle, the radio pulse is compressed, and the emission is coherent up to GHz frequencies.

B. Experimental status

Radio pulses from air showers were already detected in the 1960s [28], but progress halted due to hardware limitations and a lack of proper understanding of the radiation mechanism. It was also feared that atmospheric electric fields would have a significant and unpredictable effect on the pulse strength.

In the last decade, the interest in radio detection was revived and pursued with modern electronics [29]. LOPES demonstrated that the emission mechanism is coherent and dominantly geomagnetic in nature [30] and that only the strong electric fields inside thunderstorms can significantly affect the radiation [31].

Proof for a contribution of charge excess was found by CODALEMA [32] and later by polarization studies of AERA [25] and LOFAR [26]. CROME [33] and ANITA [34] detected GHz emission at the Cherenkov angle, which can be interpreted as relativistic compression of the air-shower radio emission. Full Cherenkov rings were found by LOFAR in the 110–190 MHz range [21].

It has been shown by LOPES that the lateral distribution of the radio signal can be used to determine X_{max} [13]. Their approach was based on a one-dimensional approximation of the radio profile, which yields a reconstruction resolution of 50 g/cm^2 for simulations and 95 g/cm^2 for LOPES data. Here, we show that a much better resolution can be achieved by using a two-dimensional profile and that modern radio simulation codes like CoREAS can accurately predict the complete radiation profile as measured by LOFAR with hundreds of antennas per individual event, providing further proof that the emission mechanism is now understood to very high detail.

C. CoREAS and CORSIKA

In this work, we use the radio simulation code CoREAS [18], which is a plugin for the particle simulation code CORSIKA [19]. CoREAS is based on a microscopic description of the radiation mechanism; i.e., it computes the contributions of each electron and positron in the shower based on the "end-point" formalism [35]. In this formalism, the radiation produced by the acceleration of a particle at the start and end point of a particle track is calculated from first principles. By summing the contributions of all particle tracks, the total emission can be calculated without making any assumptions on the type of radiation. In other words, while the radiation is best understood when explained in terms of geomagnetic and charge excess contributions, CoREAS does not simulate these components separately. Instead, it produces the complete radiation field that is generated by the distribution of charged particles simulated by CORSIKA.

We use CORSIKA 7.400, with hadronic interaction models FLUKA 2011.2b [36] and QGSJETII.04 [37]. A comparison to other interaction models is made in Sec. V B. Thinning is applied at a level of 10^{-6} with optimized weight limitation [38].

A GEANT4 [39] simulation of the LORA detectors [20] is used to convert the CORSIKA particle output into the deposited energy as a function of distance to the shower axis. The particle lateral distribution function and radio profile will be fitted to the data simultaneously.

D. Two-dimensional profiles

As explained above, the radiation profile is not rotationally symmetric and can only be accurately described by a two-dimensional intensity map. The CoREAS code computes the radio pulse for specific observer positions on the ground. A LOFAR antenna model is applied to these pulses to simulate measured waveforms. This includes applying a frequency filter (10–90 MHz) and downsampling of the signal to 200 Msamples/s. In this analysis, we use the pulse power integrated over a 55 ns time window centered at the pulse peak.

To derive a two-dimensional map, we run simulations for 160 ground positions and reconstruct the full profile by interpolation. For robust interpolation, it is necessary to choose these positions such that they cover the locations where the interference between the two radiation components reaches its minimum and maximum. This is achieved by defining a star-shaped pattern in the shower plane with eight arms, two of which are aligned with the $\mathbf{v} \times \mathbf{B}$ axis, and projecting it onto the ground. Each arm contains 20 antennas, with a spacing of 25 m in the shower plane.

In Fig. 2, the interpolation technique is demonstrated. The simulated antenna positions are marked by large
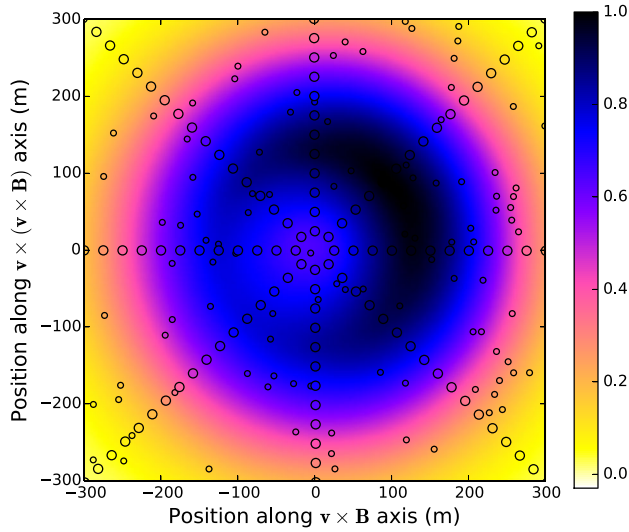
FIG. 2 (color online).   Two-dimensional profile of the received power integrated over a 55 ns window. The large circles indicate the positions for which CoREAS simulations have been generated, while the full map in the background is created by interpolation. The smaller circles indicate test positions for which simulated values are compared to interpolated values.

circles, arranged in a regular pattern. Their color reflects the total power of the pulse as received by the antenna. The interpolated radio map is indicated by the background colors. By design, the interpolated map exactly matches the values at the simulated positions. To probe the error introduced by the interpolation, we run the same simulation for two hundred additional random positions, indicated by the smaller circles. The difference between the simulated

and interpolated total power is always smaller than 2.5% of the maximum power. This error is smaller than typical uncertainties in measured power for observations with LOFAR.

Figure 3 shows the radio profiles for two showers that have been simulated with CoREAS. Both showers have a zenith angle of 49°, an azimuth angle of 171° (i.e., coming from the northwest), and an energy of 2.3×10^8 GeV. The left panel displays the radiation profile of a proton shower that has penetrated deeply into the atmosphere, while the right panel shows the profile of a much shallower iron shower. In Fig. 4, the one-dimensional lateral distribution of the power is plotted for observers along the $\mathbf{v} \times \mathbf{B}$ and $\mathbf{v} \times (\mathbf{v} \times \mathbf{B})$ axes.

Obviously, the profiles are very different. A general feature is that the power falls of more rapidly with distance for deeper showers, which is clearly seen in Fig. 4. The $X_{\max}$ reconstruction method used for LOPES is based on this feature [13,40].

However, there are also more subtle differences, like the amount of asymmetry and the position where the radiation reaches its maximum value. The method described in this paper makes use of all features of the radiation pattern by fitting the complete two-dimensional profile instead of a one-dimensional approximation.

The asymmetry along the $\mathbf{v} \times \mathbf{B}$ axis can be understood as the effect of the charge excess component. It is interesting to note that there also exists some asymmetry along the $\mathbf{v} \times (\mathbf{v} \times \mathbf{B})$ axis. This is not expected from radiation physics reviewed in Sec. III A. Indeed, when we plot the total "physical" pulse power as predicted by CoREAS, there is no asymmetry along the $\mathbf{v} \times (\mathbf{v} \times \mathbf{B})$ axis. It only appears once
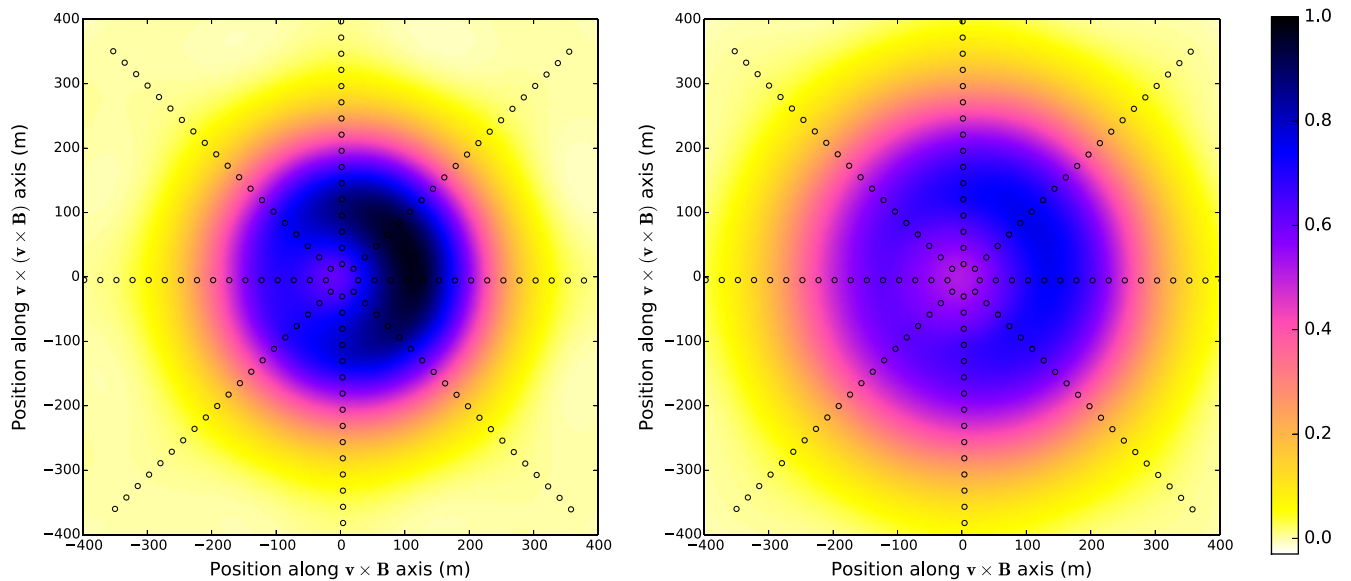

FIG. 3 (color online).   Radiation profiles of a proton shower with $X_{\max} = 794$ g/cm^2 (left panel) and an iron shower with $X_{\max} = 573$ g/cm^2 (right panel). Both showers have an energy of 2.3×10^8 GeV and a zenith angle of 49°. The circles indicate the positions that have been simulated. The full background map is created by interpolation.
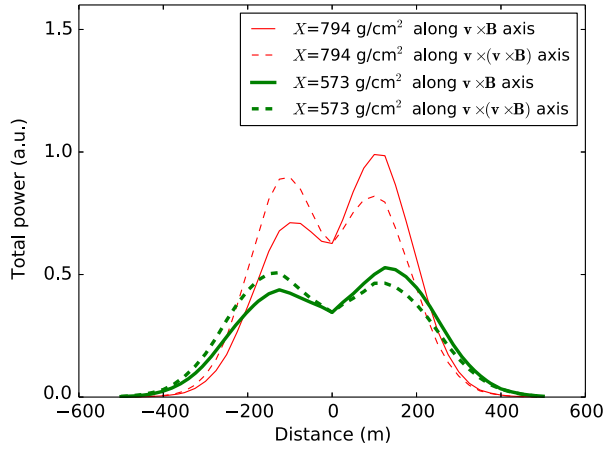
FIG. 4 (color online).   The pulse power as a function of position along the axes for the proton (red, thin) and iron (green, thick) showers shown in Fig. 3.

the antenna response model is applied to the simulated pulses to calculate the total received power. The reason for this is that for observers at different locations the radiation has a different polarization. Since the antenna gain depends on the polarization, the power received by the antenna can be different even when the original pulse power is the same. In other words, different antennas pick up a different fraction of the total pulse power.

From Figs. 3 and 4, it is clear that the shape of the radiation profile strongly depends on the atmospheric depth of the shower maximum $X_{\max}$. However, it is reasonable to assume that other variations in the longitudinal and lateral distribution of the shower also have an influence on the radiation pattern. Below, we will demonstrate that the patterns are much more sensitive to $X_{\max}$ than any other features of the shower development that vary from shower to shower. They do, however, limit the accuracy of the determination of $X_{\max}$.

E. Simulation set for LOFAR

We have developed a reconstruction technique in which simulated two-dimensional radio profiles are fitted to data. We run dedicated simulations for each shower detected by LOFAR. The shower arrival direction is reconstructed based on the arrival time of the radio pulses at all antennas [15]. An energy estimate is provided by a LORA shower reconstruction [20]. Since the shower core is often located outside the LORA array, this estimate is not accurate, and a better energy reconstruction is done at a later stage in the analysis. The core position itself is not needed as input for the simulation, since we use the star-shaped pattern of observer positions described above, instead of actual antenna positions.

For each shower in the set, we run 25 proton showers and 15 iron showers. With this amount of showers, we obtain a large range of $X_{\max}$ values that reflects the natural spread.

IV. HYBRID RECONSTRUCTION TECHNIQUE

A. Fit procedure

For each simulation, we fit the two-dimensional radiation map and the one-dimensional particle lateral distribution function to the data simultaneously, by minimizing

$$\chi^2 = \sum_{\text{antennas}} \left(\frac{P_{\text{ant}} - f_r^2 P_{\text{sim}}(x_{\text{ant}} - x_0, y_{\text{ant}} - y_0)}{\sigma_{\text{ant}}} \right)^2$$
$$+ \sum_{\substack{\text{particle} \\ \text{detectors}}} \left(\frac{d_{\text{det}} - f_p d_{\text{sim}}(x_{\text{det}} - x_0, y_{\text{det}} - y_0)}{\sigma_{\text{det}}} \right)^2, \quad (1)$$

where P_{ant} is the measured power integrated over a 55 ns window at an antenna at location $(x_{\text{ant}}, y_{\text{ant}})$ with noise level σ_{ant}, P_{sim} is the simulated power, d_{det} is the deposited energy as measured by a LORA detector at location $(x_{\text{det}}, y_{\text{det}})$ with noise σ_{det}, and d_{sim} is the simulated deposited energy. The fit contains four free parameters, two of which describe the location of the shower axis (x_0, y_0). A scaling parameter f_p for the particle lateral distribution function is needed to correct the energy scale, while a scaling parameter for the radio power f_r^2 is needed because the antennas do not yet have an absolute calibration. The radio power is approximately proportional to the square of the cosmic-ray primary energy [41], so both f_r and f_p scale linearly with energy.

B. Application to LOFAR data

Figure 5 contains the fit results for three different showers. The left panels display the radiation pattern in the shower plane. The background colors indicate the simulated radio map, while the circles indicate the measurements of the LOFAR antennas. The color of the circle represents the received power at the antenna, so the fit is of high quality when the colors of the circles blend into the background. Note that the antennas are grouped in rings: the LOFAR stations. All these showers have been detected by all six superterp stations. In addition, emission from the shower in the top row was also found in three other core stations (CS024, CS011, and CS017 in Fig. 1), and the shower in the middle row was detected by one additional station outside the superterp (CS011). For very inclined events, the antenna rings appear flattened in the event display because of the projection onto the shower plane. As explained above, for each detected shower, a total of 40 simulations is produced. The results shown here are for the simulation that yielded the fit with the lowest χ^2.

The right-hand panels of Fig. 5 show the same result in one dimension. For each antenna, the measured and simulated power is plotted as a function of distance to the shower axis. From all three examples, it is clear that the radio power is not a single-valued function of distance. Some distribution functions contain oval structures (middle and bottom row) that are reminiscent of the
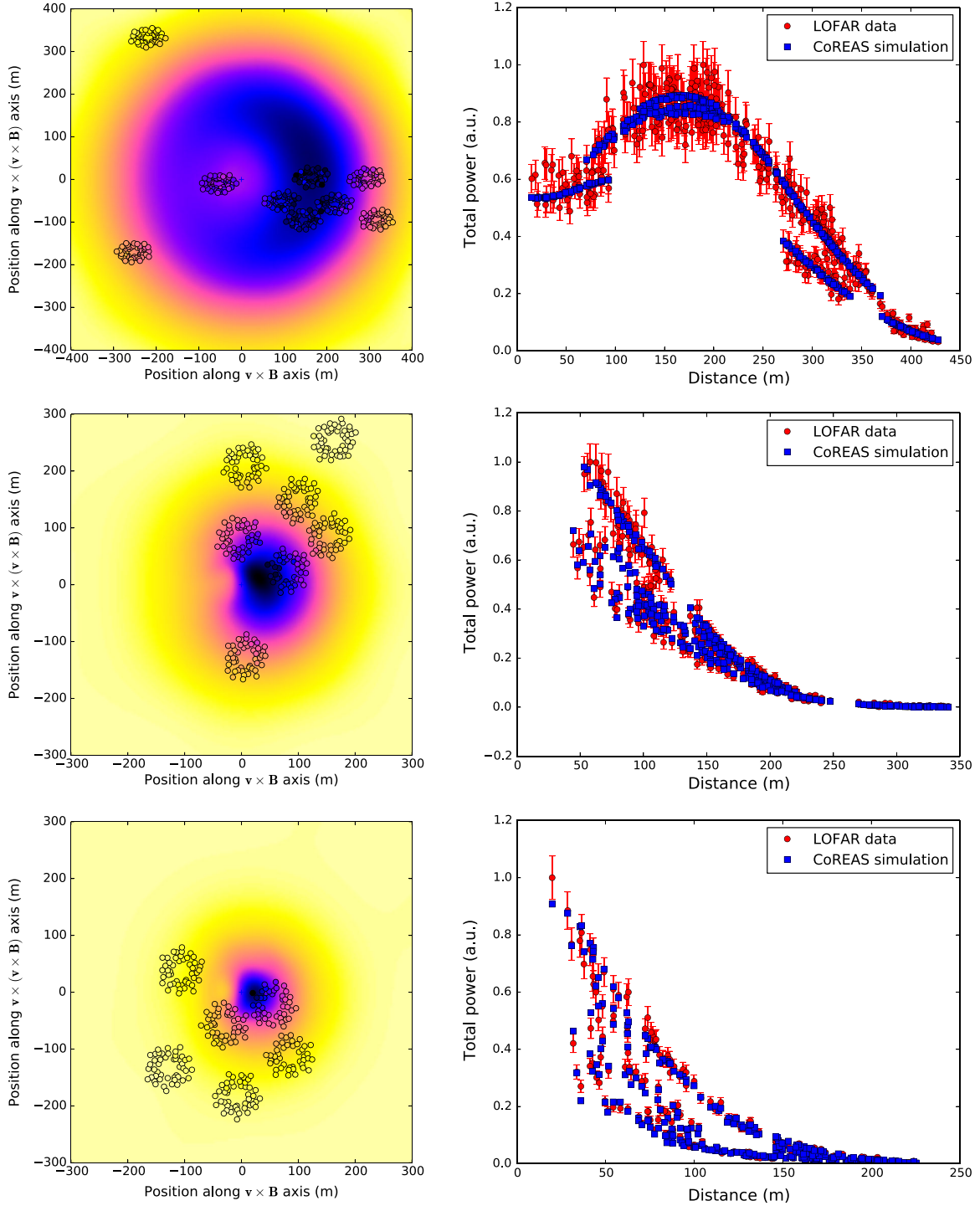
FIG. 5 (color online). Two-dimensional radio air-shower reconstructions. The measured power for three different showers (top, middle, and bottom) is fitted to a simulated radio map (left panels). The one-dimensional lateral distribution functions (right panels) are not single-valued functions of distance to the shower axis.

ring structure of the LOFAR stations. From the shower in the top row, it is clear that the position where the radio power reaches its maximum can be far from the shower axis (in this case ~150 m). As explained in Sec. III A, this is due to the interference between geomagnetic and

charge excess radiation, and Cherenkov-like propagation effects.

The fits displayed in Fig. 5 correspond to the simulation that yielded the lowest χ^2. The reduced χ^2 values for all 40 simulations that are performed per detected shower are

plotted in Fig. 6 as a function of the slanted atmospheric depth of the shower maximum X_{max}. While X_{max} is not the only shower parameter that is different between simulations because of shower-to-shower fluctuations, it is clearly the parameter that most strongly determines the quality of the fit. However, smaller effects due to other variations in the shower development introduce a "jitter." It is therefore not expected that the data points in Fig. 6 lie on a completely smooth curve.

The blue circles represent proton simulations, and the magenta squares stand for iron simulations. Proton showers on average penetrate deeper into the atmosphere than iron showers and have larger shower-to-shower fluctuations. Indeed, the proton showers cover a larger range of higher X_{max} values than the iron showers. Interestingly, in the region of overlap, the data points of the different primaries follow the same curve, at least within the uncertainty of the above-mentioned jitter. We therefore conclude that showers with the same X_{max} produce a very similar radiation pattern regardless of the mass of the cosmic-ray primary.

We fit a parabola to the data points within a 200 g/cm^2 range centered around the best-fitting simulation and regard its extremum as the reconstructed value for X_{max}. The uncertainty on this reconstructed value is determined with a Monte Carlo study (see the next section) and is different for each shower. It is tempting to derive the uncertainty from the width of the fitted parabola. However, this is only possible if the data points really follow a smooth curve. The jitter on the χ^2 values introduced by shower-to-shower fluctuations affects the shape of the parabola and therefore renders it impossible to use the width of the parabola to find the uncertainty.

C. Uncertainty on X_{max}

For each measured shower, the uncertainty on the reconstructed value for X_{max} is found by applying the following procedure to the set of simulated showers. First, one simulation is singled out, and "fake" data are produced by evaluating the radio map at the position of each LOFAR antenna and adding Gaussian noise of the same level as found in the original data. For the position of each LORA particle detector, the total deposited energy as simulated with GEANT4 is determined, and again appropriate noise is added to the signal. Then, the remaining 39 simulated showers are fitted to the fake data set using the same fitting procedure as described in Sec. IV. This yields a value X_{reco} that can be compared to the actual X_{real} of the simulated shower. Finally, the procedure is repeated for all 40 simulated showers (each time taking care that the simulation that is used to produce the fake data set is excluded from the set of simulations that is used for reconstruction).

Figure 7 shows the distribution of the $|X_{reco} - X_{real}|$ for the 40 simulations corresponding to one particular shower. We define the 1σ uncertainty as the value of $|X_{reco} - X_{real}|$ that contains 68% of the histogram. The uncertainty that is
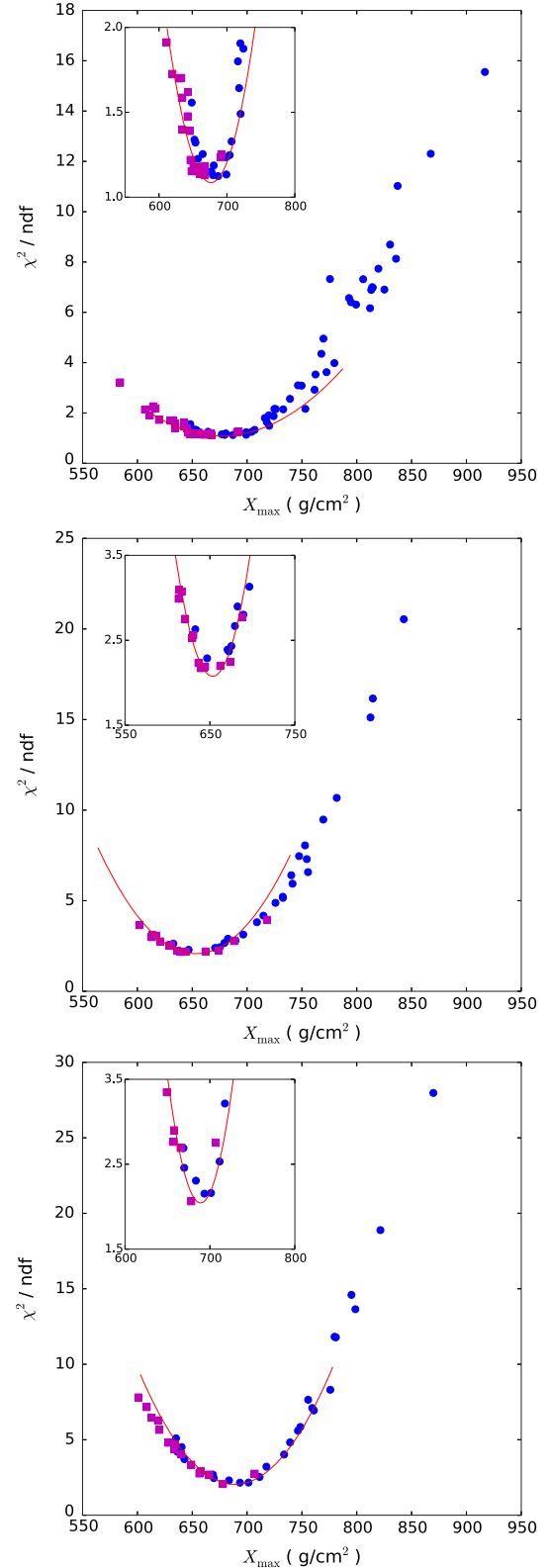

FIG. 6 (color online). Reduced χ^2 as a function of X_{max} for the same three showers as Fig. 5. The proton simulations (blue circles) and iron simulations (magenta squares) lie on the same curve, at least within the scatter. A parabola (red line) is fitted to the data points near the minimum to reconstruct X_{max}. The insets zoom in on this region.

found this way is the uncertainty due to the method σ_{meth}. There is an additional uncertainty due to the fact that the density profile of the atmosphere at the time of measurement is different from the atmospheric profile used in the CORSIKA simulation.

To correct for the atmosphere, we extract the local atmospheric density profile at the time of measurement from the Global Data Assimilation System (GDAS) [42]. We follow the approach that is used by the Pierre Auger Collaboration as described by Abreu *et al.* [43] This work also contains comparisons of atmospheric depth profiles predicted by GDAS and *in situ* measurements with weather balloons. The differences are typically smaller than 1 g/cm^2, except for altitudes very close to the ground. Since global atmospheric models typically work better in the Northern hemisphere where more weather data are available, and the geography of the northern Netherlands is rather unspectacular, we assume that the uncertainty introduced by the atmospheric model is also not worse than 1 g/cm^2 at the LOFAR site.

Because the reconstruction of $X_{\max}$ based on the radio emission profile is essentially a geometrical technique, simulations that are produced with a standard atmosphere yield the correct geometrical altitude h. The corresponding atmospheric depth is now found by evaluating

$$X(h) = \frac{1}{\cos\theta} \int_h^\infty \rho_{\mathrm{GDAS}}(h')dh', \qquad (2)$$

where ρ_{GDAS} is the atmospheric density profile as predicted by GDAS and θ is the zenith angle of the shower. Correction are typically of the order of $\sim$10 g/cm^2.
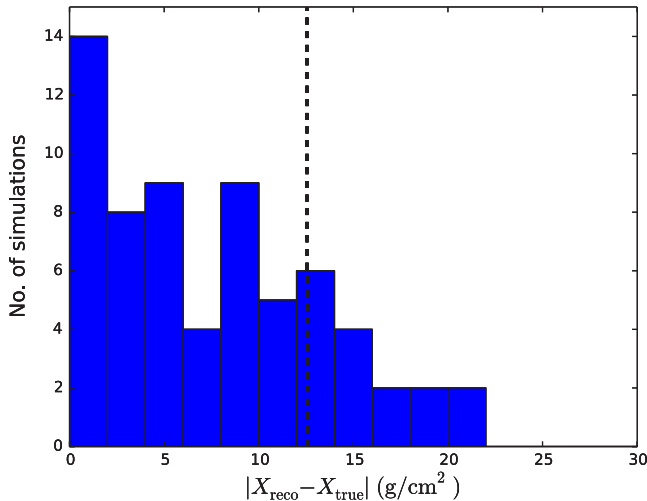

FIG. 7 (color online). The uncertainty on $X_{\max}$ for a particular shower is found by reconstructing many simulated showers and evaluating the histogram of the reconstruction error shown here. The black dotted line indicates the value that contains 68% of the histogram and is taken as the one sigma uncertainty on $X_{\max}$.
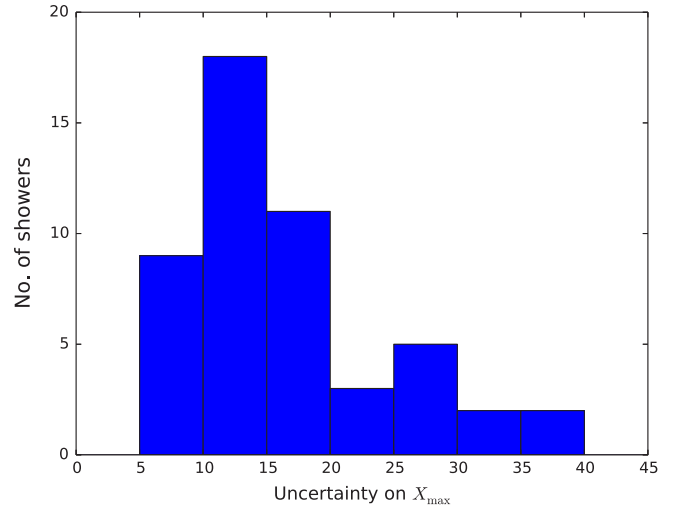

FIG. 8 (color online). Histogram of uncertainties on $X_{\max}$ for 50 sets of simulated LOFAR showers. The mean value is 17 g/cm^2.

A third contribution to the uncertainty on $X_{\max}$ comes from the uncertainty in the direction reconstruction. In this analysis, we have used a plane wave approximation that has an angular resolution of $\sim$1°, which translates into an uncertainty of $\sim$2 g/cm^2 depending on zenith angle and shower depth. Using a more realistic reconstruction based on hyperbolic wavefront shapes, the accuracy increases to $\sim$0.1° [44].

Simulation sets were generated for 50 showers (each set consisting of 25 proton and 15 iron showers). The uncertainties on $X_{\max}$ for these showers, as has been evaluated with the technique described above, are plotted in the histogram in Fig. 8. They range from 7.5 to 37.5 g/cm^2, depending on the geometry of the event, with a mean value of 17 g/cm^2.

V. SYSTEMATIC EFFECTS

In this section, we study the possible systematic effects that are introduced by the reconstruction method and the choice of models used for simulation.

A. Multivariate fit procedure

The shower simulations are fitted to the data using Eq. (1), which has four free parameters: two for the core location, one scaling factor for the radio power f_r^2, and one scaling factor for the deposited energy in the particle detectors f_p. A multivariate fit can introduce systematic biases in one or more of the fit parameters. We study this using the same approach as described in Sec. IV C. Each simulated shower is used to construct a fake data set that is reconstructed using the 39 remaining simulations made for that particular shower. For each reconstruction, the fit parameters are compared to the actual values of the simulated event. This is done for a total of 50 showers.

The results are shown in Fig. 9. The top two panels show the offset of the reconstructed core position with respect to the real core position. The left panel is a two-dimensional histogram of the core offset in which it can be seen that the core offset has no preferred direction. Hence, there is no systematic effect on the core position due to the fit procedure. The absolute value of the core offset is histogrammed in the right-hand panel. The core position is reconstructed with an accuracy of within 5 m.

The bottom panels of Fig. 9 display the distribution of the logarithm of the scaling parameters f_p and f_r^2. Since all 40 simulations of a specific shower have the same primary energy, both factors are unity when the reconstruction is perfect. Indeed, the histograms of both scaling factors are symmetric around unity. The maximum energy resolution that can be achieved with this method is given by the width of the distributions and is 15%–20%. The resolution of the radio energy scaling is slightly better than the particle energy scaling.

B. Choice of hadronic interaction model

The longitudinal development of air showers is sensitive to high-energy hadronic interactions. Hadronic cross sections, elasticities, and multiplicities cannot be calculated from first principles. Instead, phenomenological hadronic interaction models are used, which are fine-tuned to available accelerator data, but extrapolated to regimes in energy and phase space far beyond the reach of any Earth-based accelerator [45].

Differences in high-energy cross sections between models result in systematically different values for X_{max} given a certain primary mass and energy. For example, the difference in the mean atmospheric depth of the shower maximum for proton primaries as predicted by QGSJETII-04 and EPOS-LHC is of the order of 20 g/cm^2 at 10^{18} eV [46]. Since the measurement of X_{max} using the radio profile is a geometrical measurement (like fluorescence measurements), it can be argued that there is no systematic effect on the reconstructed
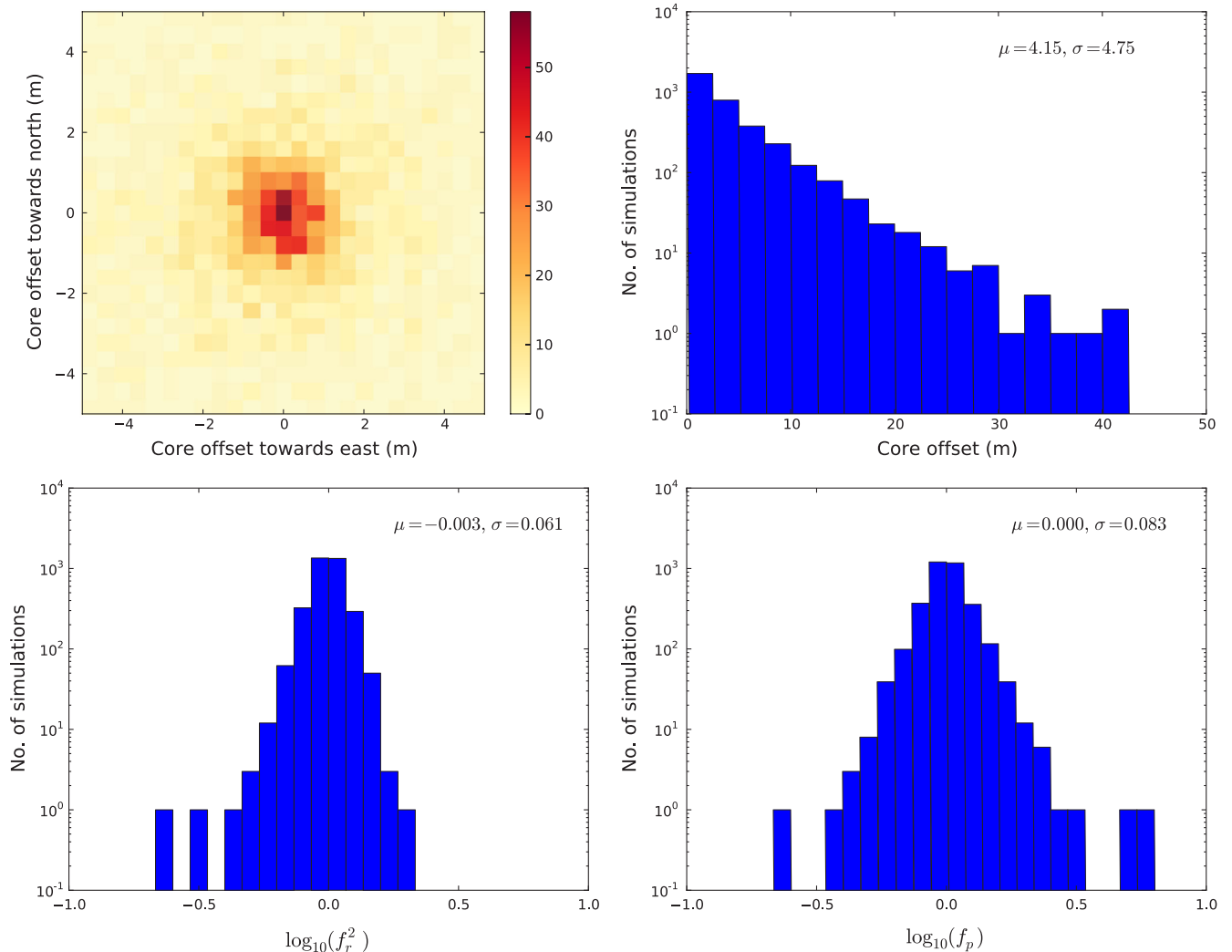

FIG. 9 (color online).　Histograms of fitting parameters for 50 showers with 40 simulations each. Top row: distribution of core offset in one and two dimensions. Bottom row: distribution of the logarithm of the scaling parameters f_r^2 and f_p.

depth due to the choice of hadronic model and that this choice only becomes essential when interpreting the data, i.e., when deriving primary mass composition from X_{max} measurements.

However, it is possible that the reconstructed value of X_{max} systematically shifts when the shapes of the longitudinal development of actual showers are different from those of the simulated showers. To evaluate this effect, we have generated shower simulations based on EPOS-LHC and SIBYLL 2.1 for ten showers and reconstructed their X_{max} values using QGSJETII-04 simulations.

The results are shown in Fig. 10. The largest systematic offset of 4.3 g/cm^2 is found for showers simulated with EPOS-LHC. Note, however, that current experimental constraints on hadronic interactions may very well allow parameter values that produce larger differences than those observed between these three particular models.

C. Choice of radio simulation code

There are currently four advanced codes that calculate the radio emission from air showers. CoREAS and ZHAireS [47] are both microscopic codes; i.e., they sum the contribution of individual electrons and positrons to obtain the total radio pulse. CoREAS is based on CORSIKA and the end-point formalism, while ZHAireS is based on Aires and the ZHS algorithm [48]. Still, both codes produce very similar results [17].

Selfas2 [49] and EVA [50] follow a more macroscopic approach, in which shower simulation codes are used to obtain histograms or parametrizations of the total charge distribution of the shower. The radiation is then calculated in a second step. A disadvantage of this approach is that the use of histograms or parametrizations may lead to the loss of information about the charge distribution. An advantage, however, is that such codes can provide a better qualitative understanding of the radiation mechanism. They can, for example, be used to calculate specific components of the total radiation (geomagnetic or charge excess), whereas the microscopic approach is oblivious to such distinctions as it calculates the radiation from first principles.

A detailed comparison of these four codes with LOFAR data is currently being made and will be the subject of a future publication. For now, we emphasize that for the example events shown here the CoREAS simulations reproduce all features observed in the data and are able to fit the data with excellent reduced χ^2 values and that CoREAS and ZHAireS produce very comparable results.

Finally, it should be understood that the correct simulation of the radio signal is mainly a numerical challenge, since the laws of electrodynamics are well known. This is in sharp contrast with the uncertainties introduced by the high-energy hadronic interactions, which can currently not be derived from first principles.
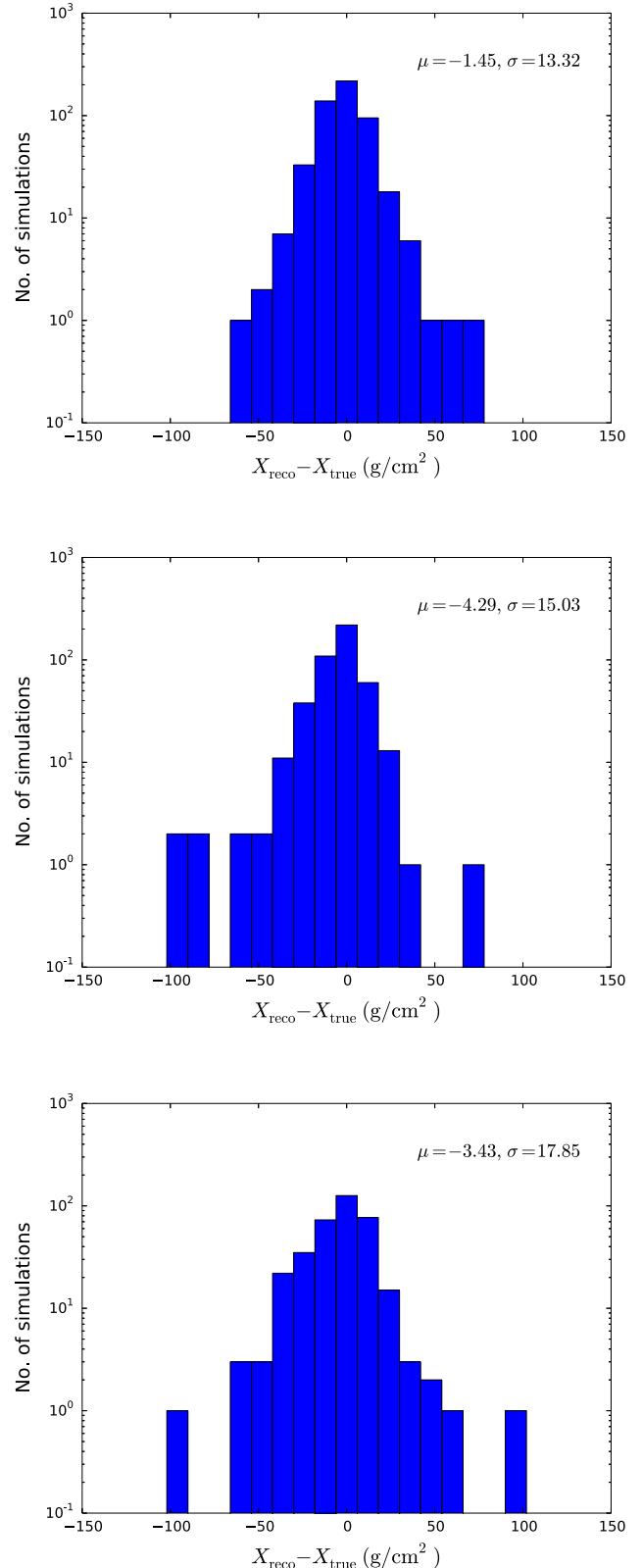

FIG. 10 (color online). Distribution of the error on the reconstructed value of X_{max} for simulations based on different hadronic interaction models (top: QGSJETII.04, middle: EPOS-LHC, bottom: SIBYLL 2.1). In each case, the reconstruction was done with a sample of QGSJETII.04 showers.

VI. CONCLUSION

We have presented a new method to reconstruct the atmospheric depth of the shower maximum X_{max} with radio measurements. It is based on the complete two-dimensional distribution of the emitted radio power that strongly depends on the longitudinal development of the shower. Application of the technique to LOFAR data yields very accurate reconstructions of typically 17 g/cm^2. This makes LOFAR an excellent observatory to study the cosmic-ray composition in the energy regime around 10^{17} eV, which may harbor the transition from a Galactic to extra-Galactic origin. We are studying the possibility of performing air-shower radio detection with the Square Kilometer Array, allowing composition study up to 10^{18} eV, as well as measurements of the p-air cross section at energies beyond the LHC scale [51].

The HEAT extension of Auger [52] performs fluorescence measurements of X_{max} in the 10^{17}–10^{18} eV range. In this regime, radio measurements with LOFAR (and SKA) will provide a second observation method that is completely independent. Compared to fluorescence detection, radio measurements depend on more complicated signal simulation and analysis techniques but suffer from fewer systematic uncertainties due to signal propagation in the atmosphere (aerosols, etc.). The techniques are thus complimentary, and a combination of them potentially leads to increased precision.

The radiation profiles that are produced with the CoREAS radio simulation code fit the data extremely well. All features in the complicated, asymmetric profiles are reproduced, and we find low reduced χ^2 values for showers that were observed with hundreds of antennas simultaneously. This inspires confidence that the radiation mechanism is now well understood and can be accurately simulated. The performance of other radio simulation codes is currently being studied and will be published separately.

We have followed a hybrid approach that combines the total radio power and particle measurements in a single fit. Because of the large number of antennas, the radio data give the dominant contribution to the fit of the shower core position. However, by including the particle detector data in the fit, we have made sure that the shower reconstruction is fully consistent with all available data.

It is possible to extend the technique to incorporate information of the radio pulse that is currently not used. The polarization and spectrum of the pulse both depend on the antenna position relative to the shower axis, and pulse arrival times can be used to fit the shower front shape leading to a higher angular accuracy.

Producing large sets of radio simulations for each detected shower requires a large amount of computational resources. The process can be streamlined by making use of a two-dimensional parametrization of the radiation profile [53,54].

Radio detection of air showers provides a new way of accurately measuring X_{max}. In contrast to fluorescence detection, it has a duty cycle of nearly 100% and may therefore be an interesting method for cosmic-ray composition studies at the highest energies. The main challenge lies in the size of the radio footprint, which is smaller than the particle footprint and requires a relatively dense antenna array. The technique itself, however, has matured and now produces accurate and robust results.

---

[1] J. Abraham *et al.* (Pierre Auger Collaboration), Phys. Rev. Lett. **101**, 061101 (2008).

[2] R. U. Abbasi *et al.* (HiRes collaboration), Phys. Rev. Lett. **100**, 101101 (2008).

[3] K. Greisen, Phys. Rev. Lett. **16**, 748 (1966).

[4] G. Zatsepin and V. Kuzmin, JETP Lett. **4**, 78 (1966).

[5] K.-H. Kampert and M. Unger, Astropart. Phys. **35**, 660 (2012).

[6] J. Abraham *et al.* (Pierre Auger Collaboration), Science **318**, 938 (2007).

[7] J. Abraham *et al.* (Pierre Auger Collaboration), Nucl. Instrum. Methods Phys. Res., Sect. A **620**, 227 (2010).

[8] H. Tokuno *et al.* (Telescope Array Collaboration), Nucl. Instrum. Methods Phys. Res., Sect. A **676**, 54 (2012).

[9] W. Apel *et al.* (KASCADE-Grande Collaboration), Phys. Rev. D **87**, 081101 (2013).

[10] M. G. Aartsen *et al.* (IceCube Collaboration), Phys. Rev. D **88**, 042004 (2013).

[11] S. F. Berezhnev *et al.* (Tunka Collaboration), in *Proceedings of the 32nd International Cosmic Ray Conference (ICRC2011), 2011, Beijing, China*, Vol. 1, p. 209, http://www.ihep.ac.cn/english/conference/icrc2011/paper/proc/v1/v1_0250.pdf.

[12] W. Apel *et al.* (LOPES Collaboration), Phys. Rev. D **85**, 071101 (2012).

[13] W. Apel *et al.* (LOPES Collaboration), Phys. Rev. D **90**, 062001 (2014).

[14] M. P. van Haarlem *et al.* (LOFAR Collaboration), Astron. Astrophys. **556**, A2 (2013).

[15] P. Schellart *et al.* (LOFAR Collaboration), Astron. Astrophys. **560**, A98 (2013).

[16] H. Falcke and P. W. Gorham, Astropart. Phys. **19**, 477 (2003).

[17] T. Huege, M. Ludwig, O. Scholten, and K. D. de Vries, Nucl. Instrum. Methods Phys. Res., Sect. A **662**, S179 (2012).

[18] T. Huege, M. Ludwig, and C. W. James, AIP Conf. Proc. **1535**, 128 (2013).

[19] D. Heck, J. Knapp, J. N. Capdevielle, G. Schatz, and T. Thouw, https://web.ikp.kit.edu/corsika/physics_description/corsika_phys.html.

[20] S. Thoudam *et al.* (LOFAR Collaboration), arXiv:1408.4469.

[21] A. Nelles *et al.* (LOFAR Collaboration) (to be published).

[22] F. D. Kahn and I. Lerche, Proc. R. Soc. A **289**, 206 (1966).

[23] G. A. Askaryan, J. Exp. Theor. Phys. **14**, 441 (1962).

[24] K. D. de Vries, O. Scholten, and K. Werner, Astropart. Phys. **45**, 23 (2013).

[25] A. Aab *et al.* (Pierre Auger Collaboration), Phys. Rev. D **89**, 052002 (2014).

[26] P. Schellart *et al.* (LOFAR Collaboration), J. Cosmol. Astropart. Phys. (to be published).

[27] K. D. de Vries, O. Scholten, and K. Werner, Astropart. Phys. **45**, 23 (2013).

[28] J. V. Jelley, J. H. Fruin, N. A. Porter, T. C. Weekes, F. G. Smith, and R. A. Porter, Nature (London) **205**, 327 (1965).

[29] T. Huege, Braz. J. Phys. (to be published).

[30] H. Falcke *et al.*, Nature (London) **435**, 313 (2005).

[31] S. Buitink *et al.* (LOPES collaboration), Astron. Astrophys. **467**, 385 (2007).

[32] V. Marin *et al.* (CODALEMA Collaboration), in *Proceedings of the 32nd International Cosmic Ray Conference (ICRC2011), 2011, Beijing, China*, Vol. 1, p. 291.

[33] R. Šmída *et al.* (CROME Collaboration), EPJ Web Conf. **53**, 08010 (2013).

[34] S. Hoover *et al.* (ANITA Collaboration), Phys. Rev. Lett. **105**, 151101 (2010).

[35] C. James, H. Falcke, T. Huege, and M. Ludwig, Phys. Rev. E **84**, 056602 (2011).

[36] G. Battistoni, F. Cerutti, A. Fassò, A. Ferrari, S. Muraro, J. Ranft, S. Roesler, and P. R. Sala, AIP Conf. Proc. **896**, 31 (2007).

[37] S. Ostapchenko, Nucl. Phys. B Proc. Suppl. **151**, 147 (2006).

[38] M. Kobal *et al.* (Pierre Auger Collaboration), Astropart. Phys. **15**, 259 (2001).

[39] S. Agostinelli *et al.*, Nucl. Instrum. Methods Phys. Res., Sect. A **506**, 250 (2003).

[40] T. Huege, R. Ulrich, and R. Engel, Astropart. Phys. **30**, 96 (2008).

[41] T. Huege and H. Falcke, Astropart. Phys. **24**, 116 (2005).

[42] NOAA Air Resources Laboratory (ARL), Global Data Assimilation System (GDAS1) Archive Information, Tech. Rep. (2004).

[43] P. Abreu *et al.* (Pierre Auger Collaboration), Astropart. Phys. **35**, 591 (2012).

[44] A. Corstanje *et al.*, Astropart. Phys. **61**, 22 (2015).

[45] R. Ulrich, R. Engel, and M. Unger, Phys. Rev. D **83**, 054026 (2011).

[46] T. Pierog, J. Phys. Conf. Ser. **409**, 012008 (2013).

[47] J. Alvarez-Muñiz, W. R. Carvalho, and E. Zas, Astropart. Phys. **35**, 325 (2012).

[48] E. Zas, F. Halzen, and T. Stanev, Phys. Rev. D **45**, 362 (1992).

[49] V. Marin and R. Benoît, Nucl. Instrum. Methods Phys. Res., Sect. A **662**, S171 (2012).

[50] O. Scholten, K. Werner, and F. Rusydi, Astropart. Phys. **29**, 94 (2008).

[51] T. Huege *et al.*, arXiv:1408.5288.

[52] E. Varela *et al.* (Pierre Auger Collaboration), J. Phys. Conf. Ser. **468**, 012013 (2013).

[53] A. Nelles, S. Buitink, H. Falcke, J. R. Hörandel, T. Huege, and P. Schellart, Astropart. Phys. **60**, 13 (2015).

[54] J. Alvarez-Muñiz, W. Carvalho, H. Schoorlemmer, and E. Zas, Astropart. Phys. **59**, 29 (2014).